Critical behavior of coupled ^{4}He regions near the superfluid transition

Justin K. Perron, Mark O. Kimball, Kevin P. Mooney, and Francis M. Gasparini
University at Buffalo, The State University of New York, Buffalo, New York 14260, USA
(Received 5 December 2012; revised manuscript received 28 January 2013; published 11 March 2013)

Proximity and coupling effects between contiguous regions of ^{4}He are expected to occur over a distance on the order of the temperature-dependent correlation length $\xi(t)$. We present recent measurements of ^{4}He confined in arrays of $(2\ \mu\text{m})^3$ boxes linked through a ^{4}He film. The specific heat and superfluid fraction of the ^{4}He in these geometries reveal effects which occur at distances much larger than expected. These effects include enhancements in specific heat and superfluid fraction as well as shifts in the temperatures of the superfluid onset and specific-heat maximum. Our analysis gives evidence for the relevance of the finite-size correlation length $\xi(t,L)$ in explaining these effects even though the effects occur at distances over an order of magnitude larger than $\xi(t,L)$. These results can be used to deduce the finite-size scaling locus for $\xi(t,L)$. The spatial distance over which coupling and proximity effects are observed raises questions regarding the physical mechanism for these effects and the interpretation of $\xi(t)$. Lastly, these results are discussed in connection to other measurements of ^{4}He in confined geometries, and the relevance to other critical systems.

DOI: 10.1103/PhysRevB.87.094507 PACS number(s): 64.60.an, 74.45.+c, 67.25.dj, 67.25.dp

I. INTRODUCTION

The critical behavior of ^{4}He at the superfluid transition has been extensively studied.[1,2] The behavior in the thermodynamic limit has been well documented in a variety of experiments. Thus, the critical exponents for the specific heat, superfluid density, and, indirectly, the correlation length have all been obtained (see Ref. 1 for an early review and Ref. 2, Sec. II for a more recent review). Theoretical calculations of the XY model yield exponents which are of comparable, if not better, precision to experimental results.[3] Although there are some small discrepancies, one might say that critical behavior has been well tested in the thermodynamic limit and there is good agreement with theoretical expectations.

^{4}He has also been studied when confined in a variety of heterogeneous media from packed powders to porous glasses. In general, one finds that these studies yield data which are unique to each particular confinement.[4,5] In the case of uniform confinement, most extensively for films formed between two parallel surfaces representing two-dimensional (2D) crossover, finite-size scaling has been tested over a wide range of film thickness.[2] These measurements, which use the thickness of the films as an independent scaling variable, also yield more directly from finite-size scaling the value of correlation length exponent. In the bulk limit, this is obtained indirectly from the superfluid density.

Experiments have also been done with ^{4}He in arrangements whereby two bulk regions of fluid are separated by small openings or weak links.[6,7] These links are "weak" because near the bulk transition temperature T_λ, their size, both length and traverse dimension, becomes comparable to the temperature-dependent correlation length which diverges at the transition T_λ as

$$\xi^{\pm} = \xi_0^{\pm}\left|1 - \frac{T}{T_\lambda}\right|^{-\nu} \equiv \xi_0^{\pm} t^{-\nu}. \tag{1}$$

The amplitudes $\xi_0^- = 0.343$ nm (Ref. 8) and $\xi_0^+ = 0.143$ nm below[9–11] and above[12] T_λ, respectively. The correlation-length exponent is $\nu = 0.6705$.[11] These experiments verified that Josephson effects could be seen in ^{4}He as they have been seen in low-temperature superconductors,[13] and in superfluid ^{3}He.[14] The results for ^{4}He are very significant because the effects are manifest only in the critical region and in the presence of fluctuations of the same spatial extent as the weak links themselves. This is unlike the low-temperature superconductor and ^{3}He, which have values of ξ_0 orders of magnitude larger than ^{4}He, and where fluctuations play no significant role. Thus, in these cases tunneling and weak link effects can be seen well away from the superconducting or superfluid transition temperature. Theoretical considerations about Josephson effects in ^{4}He were made by Mamaladze and Cheishvili[15] very early after the observations with superconductors. In their work, they use mean-field theory to explore the coupling between two regions of bulk liquid, or in other words, proximity effects of bulk liquid on ^{4}He confined in a slit.

A different type of experiment can be done with ^{4}He whereby one uses a weak link to connect two regions which are not bulk but have a finite, relatively large, spatial dimension. Two variables can now be changed: the size of the coupled regions and the strength of the weak link. Information can now be obtained about the strength of the coupling between the large regions through the weak link, as well as thermodynamic information about the weak link itself, modified, as one might expect, by the presence of the larger regions. One might call the latter a proximity effect of the large region on the weak link. Experiments on Josephson effects do not yield such information, nor are they designed to do so. These coupling and proximity effects are more generic than just for liquid ^{4}He and should pertain to any continuous transition near the critical point subject to equivalent conditions. The general problem is one of variation of the order parameter and other thermodynamic functions from one region to another, and how these are influenced by neighboring ordering regions and inherent critical fluctuations. These regions might have close, but different, transition temperatures due, for instance, to chemical doping or because of spatial constraints. One might well expect that these effects would be manifest on the scale of the temperature-dependent correlation length. However, if the coupled regions are both finite and one is characterized by a small dimension L, it is not the bulk correlation length which is

relevant, but one suitably renormalized for finite-size effects, $\xi(t,L)$. We are unaware of any prior measurements of this type of coupling in any system at a continuous transition. We note that the establishment of coupling and proximity effects relies on knowing the bulk behavior and, more importantly, on knowing the behavior of the system uniformly confined but in isolation whereby such effects are absent.

The measurements of specific heat and superfluid density we are reporting are for systems consisting of an array of boxes of ^{4}He with $(2\ \mu\text{m})^3$ volume and linked by, or in equilibrium with, a uniform film 33 nm thick. We vary, in separate experimental cells, the separation among the boxes but keep the film at the same nominal thickness. Thus, our system consists of dots of helium which, as $\xi(t,L)$ grows, crosses over to 0D and, a film which crosses over to 2D. These measurements build on data in which boxes of ^{4}He in $(2\ \mu\text{m})^3$ and $(1\ \mu\text{m})^3$ boxes where studied while connected through narrow channels of different size, thus weak links of different strength.[16,17] This work quantifies these earlier observations by using a simplified confinement geometry where there are no channels and each box is connected to its neighbors in a more controlled and quantifiable way. What we find is that the mutual influence between two different connected regions in which the helium is confined extends to distances more than an order of magnitude larger than $\xi(t)$ and perforce at even much larger distances than $\xi(t,L)$. This is very surprising, considering that the meaning attributed to the correlation length near a critical point is the distance over which information is transferred,[18] or the distance to which order propagates.[19] Thus, correlations or information, such as ordering, between separate regions are expected to decay exponentially with the ratio of distance to $\xi(t)$. Some of the work reported here has appeared in other brief publications.[20–23] Here, we report new data and analysis and summarize all of these results in a comprehensive way.

This paper is organized as follows: In Sec. II, we describe the construction of the experimental cells and our measuring techniques. This is followed by results and finite-size scaling analysis of a uniform 33-nm film. Data for ^{4}He in boxes and connected through a 33-nm film are then presented and analyzed for coupling and proximity effects. We also present data for the superfluid density of an 8.7% concentration of ^{3}He in ^{4}He that are relevant to the issue of coupling and proximity effects. We conclude with a discussion of how these results are relevant to other measurements of ^{4}He in confined geometries, and other critical systems.

II. EXPERIMENTAL DETAILS

A. Confinement cell and cryostat

The measurements reported in this paper were performed on ^{4}He confined between two silicon wafers, each with a patterned thermal oxide. The fabrication of the wafers, from oxide growth to etching, is performed at the Cornell Nanoscale Science and Technology Facility.[24]

The top wafer, which defines the film region of the confinement, is a 2-inch [100] single-crystal silicon wafer 375 μm thick. The wafer is cleaned in standard RCA acid and base baths before the native oxide is removed in a 20:1 hydrofluoric acid (HF) bath.[25] Immediately following this, a dry thermal oxide growth is performed resulting in a nominally 33-nm oxide. The standard deviation in oxide thickness across an individual wafer is about 1 nm as measured by ellipsometry. The wafers are then spun with photoresist before being exposed with a contact aligner. The unexposed regions include a 4-mm border along the perimeter of the wafer, an array of $(100\ \mu\text{m})^2$ squares throughout the wafer and a $(8\text{-mm})^2$ central region of 15-μm-wide channels. These channels are a technical necessity for the precision of our measurement but are unimportant to the scope of this paper.[26] Finally, the exposed regions are wet etched away using 30:1 buffered oxide etch and the residual resist is removed. This leaves a bare silicon wafer with a border of oxide to act as a seal on the confinement cell, an array of $(100\ \mu\text{m})^2$ by 33-nm oxide posts which will act as support pillars keeping the separation between the wafers uniform while bonding, and the previously discussed central region.

The bottom wafers, which define the box geometries, are prepared with the same RCA clean/HF bath procedure before a wet thermal growth is performed. This leaves a nominally 2-μm-thick oxide[27] with a $\sim$1-nm standard deviation in thickness across the wafer similar to that observed in the top wafers. Processing the $(2\ \mu\text{m})^3$ boxes in the oxide is more complicated than the contact exposure and wet etching used for the top wafers. A mask for a 5$\times$ reduction stepper must be designed to expose the array of boxes. Since the spacing between boxes is small (2–4 μm), an optical proximity effect causes the exposed features to be larger than one may expect from a simple 5$\times$ reduction. This growth of the features is different for each box spacing and must be adjusted for in the mask design. Once an appropriate mask has been made, it is stepped across the wafer exposing the box pattern in photoresist. To achieve the necessary vertical side walls in such a thick oxide, a CHF_3/O_2 reactive ion etch is performed. The initial etch rates are calculated from the rates in unpatterned oxide, however, the rate for open oxide differs from that in the small features. Therefore, after the first attempt is etched, the wafer is then cleaved and examined under a scanning electron microscope (SEM) to determine the correct etch rate. An example of such a micrograph is shown in Fig. 1(a). The new rate is used to etch another pattern in a separate growth; this wafer is also cleaved to ensure that the oxide is etched down to the bare Si in the box regions. Finally, a third wafer, to be used in the measurement, is fully processed with the appropriate etch times and characterized with an SEM as seen in Fig. 1(b). All processed wafers are given a final cleaning in an O_2 plasma for about 10 min. This removes all traces of residual resist. We found this to be necessary in order to obtain good wafer bonding.

Once the wafers have been processed, they are brought back to our laboratory to complete the cell fabrication. A 0.029 inch diameter diamond drill bit is used to make a small filling hole in the center of the top wafer. This will be used to introduce ^{4}He into the cell. The wafers are then RCA cleaned and rinsed with deionized water before direct wafer bonding.[28] Once bonded, the wafers form a cavity between them with the geometry shown, not to scale, in Fig. 2. In this figure, the larger squares are the oxide posts belonging to the top wafer and the gray region is the oxide belonging to the bottom wafer.

Once the bonded cell is formed, a Constantan[29] film heater is evaporated on the bottom wafer. The heater pattern has three

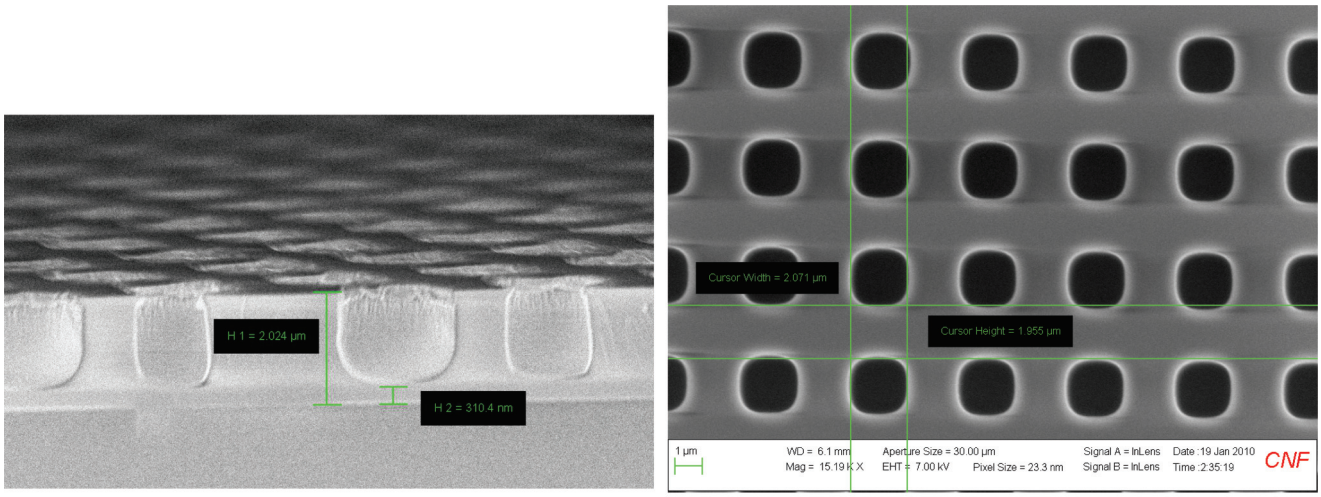

(a) cleaved wafer used to determine etch rates

(b) SEM micrograph used to characterize boxes

FIG. 1. (Color online) SEM micrographs used to calculate etch rates and characterize the boxes (see text for details).

different current paths allowing the use of two independent heaters at any one time. A filling line is epoxied to the cell via a cylindrical silicon slug of 8 mm diameter with an axial hole. The large slug is robust enough to withstand the difference in thermal contractions between the metal filling line and the silicon, thus preventing any unwanted stress on the fragile wafers. The filling line consists of a copper flange that will eventually attach to the cryostat via an indium O-ring, a stainless steel (ss) tube soldered to a second copper piece also soldered to a thin ss sleeve which is epoxied to the slug. Lastly, two doped germanium thermometer chips and several indium heat sinks are epoxied on the top wafer. A cartoon showing the final arrangement of the confinement cell is shown as an inset in Fig. 3. Once assembled, the filling line is attached to a stage (S1) of the cryostat with an indium O-ring. A valve is located on S1 which isolates the cell from the rest of the filling line. Indium heat sinks (not shown in the figure) are attached via a copper wire to a second stage (S2) of the cryostat. Both S1 and S2 contribute to the temperature stability and control of the cell as discussed in the following.

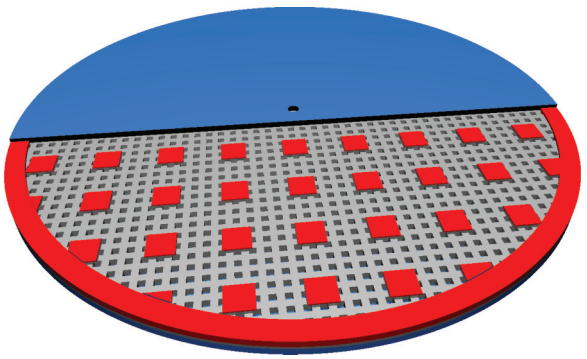

FIG. 2. (Color online) A cartoon cut-away view (not to scale) of two bonded wafers. See text for details of the features.

B. Temperature control

The S1 and S2 stages are both individually temperature controlled using a Proportional, Integral and Differential (PID) feedback loop between an encapsulated Ge thermometer and an Ohmic heater via a four-terminal ac bridge with the standard at low temperatures. A seven decade ratiotransformer (ratiotran) is used as the balancing element. Null is detected with a lock-in amplifier. The temperature of S1 is held slightly higher than S2 causing the temperature of the confinement cell to naturally fall between the two. The cell's temperature is further regulated with one of its thermometers and a similar bridge arrangement and PID feedback loop. This regulates the short-term fluctuations of the cell to about 1 μK with no visible long-term drifts over the time of data acquisition.

^{4}He is condensed through the filling line into the confinement cell. To determine the absolute temperature and, more importantly, the bulk transition temperature T_λ, excess ^{4}He is intentionally condensed forming a puddle of bulk liquid in the

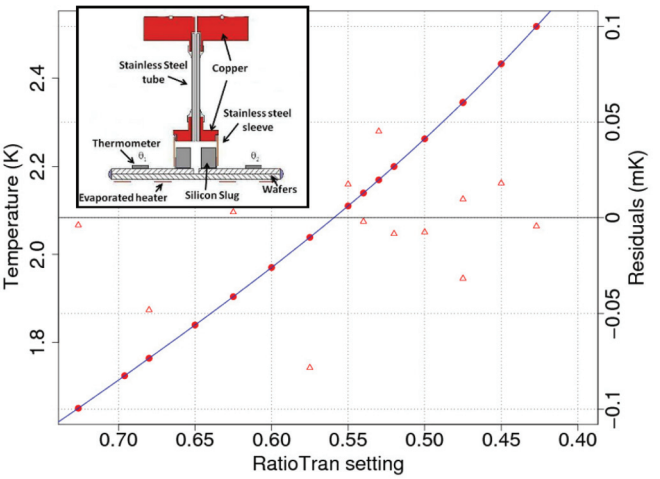

FIG. 3. (Color online) An example of the temperature calibration of a Ge thermometer. Plotted on the right vertical axis (triangles) are the residuals of the fitted temperature function. The inset is a cartoon of an assembled confinement cell and filling line.

silicon slug. The vapor pressure of this liquid is measured while regulating its temperature via the cell's feedback loop. After a thermomolecular correction,[30] the vapor pressure is converted to a temperature using the ITS-90 temperature scale.[31] The temperature is then used to calibrate the cell thermometers. The temperature is fit to a polynomial as a function of ratiotran setting. An example is shown in Fig. 3 along with the residuals of the fit. The data scatter within a band of $\pm 50\ \mu$K. The bulk transition temperature T_λ is determined *in situ* as well by allowing the temperature of the cell to drift slowly and observing a kink in the drift rate. This kink corresponds to the rapid increase in heat capacity resulting from the bulk helium above the cell going through its specific-heat maximum. Using the temperature scale and the measurement of this kink, we are able to determine T_λ within $\sim \pm 2\ \mu$K. This determination is more relevant than the absolute temperature since all of the analysis is in the critical region, i.e., the reduced temperature $t = |T - T_\lambda|/T_\lambda$ is the important variable.

C. Heat capacity and superfluid fraction

For both heat-capacity and superfluid density measurements, the confinement cell is regulated as discussed above to an average cell temperature T_θ. In the heat-capacity measurement, a second heater path is used to induce small temperature oscillations about T_θ. Using a lock-in amplifier and a second thermometer, one can measure the amplitude of these oscillations. Typically, by averaging over several minutes, these oscillations can be resolved to better than 50 nK. Knowing the power through the heater and the magnitude of the temperature oscillations one can determine the heat capacity. Equations for the frequency response are given in Ref. 26. The empty confinement cell is measured over a large temperature region before being filled with ^{4}He. Typical values for this heat capacity are in the 40–60 μJ/K near T_λ and measured to within $\pm 0.3\%$. This background measurement is subtracted from the filled cell measurement leaving only the heat capacity of the confined ^{4}He. The precise knowledge of the confinement volume afforded by the nanofabrication allows the number of moles of ^{4}He to be calculated and therefore the specific heat. Far from T_λ, the result should match the bulk data since in this temperature region finite-size effects are too small to observe. This is ensured by multiplying all data by a normalization factor on the order of 1% which accounts for the uncertainties in determining the absolute value of the specific heat. The above measurement technique is described in more detail in Ref. 26.

Our measurements of heat capacity involve using a heat flux through the confined helium. There are two effects which come into play in this case which would not be of concern in an adiabatic measurement. First, the transition temperature in bulk helium is affected by a heat flux as reported for instance in Refs. 32 and 33. This would add to effects of finite size and coupling which are our primary concerns. Specifically, one finds that the shift in transition temperature due to a power flux Q through the helium is given by[32]

$$t_c(Q) = \frac{T_\lambda - T_c(Q)}{T_\lambda} = \left(\frac{Q}{Q_0}\right)^x, \tag{2}$$

where experimentally one finds $x = 0.813 \pm 0.012$; $Q_0 = 568 \pm 200$ W/cm^2. Theoretically, one has $x = 1/2\nu \simeq 0.75$; $Q_0 = 6572$ W/cm^2. This is discussed in Ref. 34. In our measurements, we typically vary the amplitude of the temperature oscillations using higher amplitudes away from the transition and smaller amplitudes closer in. The maximum rms temperature oscillations are about 10 μK for $|T - T_\lambda| > 10^{-4}$ K and 2 μK for the region closer to the transition. For the cells of box confinement, the frequency of temperature oscillations is in the range of 42–83 Hz. To achieve the above temperature amplitudes, different power fluxes are used. Closest to the transition we used a maximum total power which for the various cells is in the range of (1.5–2.2) μW. This includes the power used to regulate the average temperature of the cell. The heaters are patterned spirals of copper nickel alloy evaporated on the bottom of the cell which is 5 cm in diameter. These powers yield a corresponding heat flux in the range of (0.071–0.11) μW/cm^2 in the region closest to the transition. Equation (2), with the experimental parameters, yields a shift of the transition temperature due to the largest flux of $t_c(0.11\ \mu\text{W/cm}^2 = 1.3 \times 10^{-8}$. This shift is even smaller if one uses the theoretical parameters. Thus, the shift due to the measuring power is too small to influence our data. The second effect due to a finite flux through the helium is an enhancement of the specific heat ΔC_Q. This can be written as follows:[34]

$$\Delta C_Q t^\alpha = A(Q/Q_c)^2, \tag{3}$$

where Q_c is obtained by inverting Eq. (2) for any temperature t, $A = 69 \pm 4$ J/mol K, and $\alpha = -0.0115$ (see below). For $t = 10^{-6}$, we find using $Q_0 = 6571$ W/cm^2 a value of $Q_c = 6.57 \times 10^{-5}$ W/cm^2 and hence at $t = 10^{-6}$ a heat-capacity enhancement of 1.6×10^{-4} J/mol K. This is also a negligible effect for our measurements.

The superfluid fraction ρ_s/ρ measurement is very similar to the heat-capacity technique. The cell is regulated at T_θ and a second heater is used to impose an oscillatory temperature. However, unlike in the heat-capacity measurement, the frequency is varied. During the heating portion of the temperature oscillations, the chemical potential μ in the cell increases relative to that of the bulk in the filling line. As a result, superfluid flows into the cell from the filling line. The normal fluid counterflow is prevented because the spatial confinement of the cell is smaller than the viscous penetration length. With the normal fluid stationary, the influx of superfluid causes an increased pressure; this acts as the restoring force driving the superfluid back out of the cell during the cooling portion of the temperature oscillation. This process results in a Helmholtz resonance between the ^{4}He in the confinement and the bulk ^{4}He in the filling line. The resonant frequency is proportional to $\sqrt{\rho_s/\rho}$, which is characteristic of the smallest confinement region. In the case of the cells discussed here, this region is the filling film. By varying the drive frequency of the heater and recording the resultant temperature oscillations, the resonance can be easily identified. It is also identified in the phase difference between the drive and pickup signals. The equations for these line shapes as well as a more complete description of this "adiabatic fountain resonance" (AFR) measurement technique are found in Ref. 35.

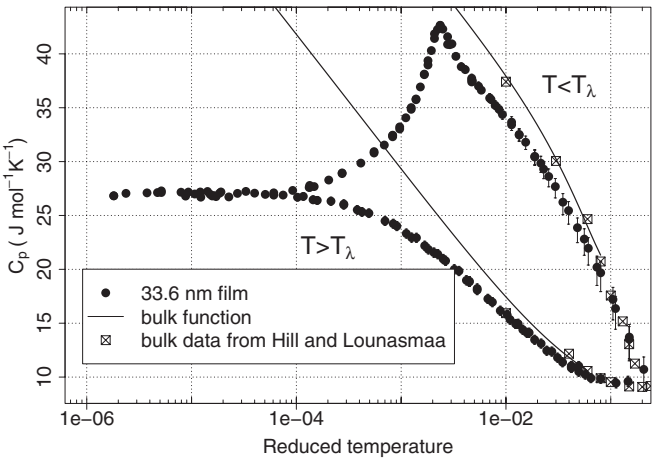

FIG. 4. The specific heat of the 33.6-nm film analyzed using the measured oxide thickness as the ^{4}He film thickness. The solid lines are for the bulk specific heat. The square symbols are from Ref. 40 and extend the comparison outside the critical region.

III. RESULTS AND ANALYSIS

A. 33-nm film

We begin the experimental results by discussing the measurements of a uniform film. In this confinement, the bottom wafer was not patterned. The top wafer's oxide thickness was measured using ellipsometry to be 33.6 ± 0.98 nm and patterned with the top wafer features discussed in the previous section. The specific heat of the helium in this confinement is shown in Fig. 4. Also plotted are solid lines indicating the bulk specific heat in the critical region using a function given in Ref. 26 which represents data from four different sets of measurements.[36–39] Also shown, as boxed symbols, are bulk data from Ref. 40 which extend beyond the critical region. The current data were analyzed using the measured oxide thickness of 33.6 nm as the ^{4}He film thickness. When analyzed this way, the normalization to bulk required a 9% correction, which is unusually high and beyond what we can attribute to uncertainties in electronic gains, geometry of the cell, and temperature scale. Revisiting the assumption that the ^{4}He film is accurately characterized by the grown oxide thickness, we discovered that it is necessary to take into account the native oxide which, although traditionally believed to be <2 nm, has been reported recently[41,42] at over 4 nm depending on the chemical treatment of the silicon. Reanalyzing the data as a 30-nm film did not change the result in a significant way, but does require only a 2% normalization to agree with bulk behavior far from T_λ. This is much more in line with results with other experimental cells.

We further checked the resulting specific heat against finite-size scaling as described in Ref. 2. To do this, one needs to calculate the following quantity:

$$[C(t,\infty) - C(t,L)]t^\alpha \equiv \Delta C_p t^\alpha = g_1(tl^{1/\nu}), \qquad (4)$$

where $\alpha = -0.0115$ is the critical exponent of the bulk specific heat.[43] This quantity $\Delta C_p t^\alpha$ is expected to fall on a universal locus[19,39,44] as a function of the variable $L/\xi(t)$ or, equivalently, $t(l)^{1/\nu}$, with $l = L/\xi_0$. The results, plotted in Figs. 5 and 6 for $T > T_\lambda$ and $T < T_\lambda$, respectively, show that the 30-nm analysis is much more consistent with previous results. When analyzed as a 33.6-nm film, the data fall somewhat higher than the locus defined by previous planar ^{4}He data, most obviously at large values of the scaling variable. When analyzed as a 30-nm film, the data lie exactly on the average locus of the other data. This persists until the region of the specific-heat maximum indicated by the minimum in Figs. 6(a) and 6(b) where scaling for all data breaks down. The better agreement of the specific-heat scaling is mirrored in the single-point scaling results for the magnitude of the specific heat at T_λ, as well as the shift of the maximum and the value of the specific heat at the temperature t_0 where $\xi(t_0) = L$. These results are discussed in greater detail in Refs. 45 and 23.

The above discussion of scaling and the normalization of the data both indicate that the true thickness of the ^{4}He film is closer to 30 nm than 33.6 nm. However, the films discussed in future sections, used for linking ^{4}He in box geometries, can not be tested against scaling, thus can not be analyzed and checked in this way. However, this is irrelevant to our

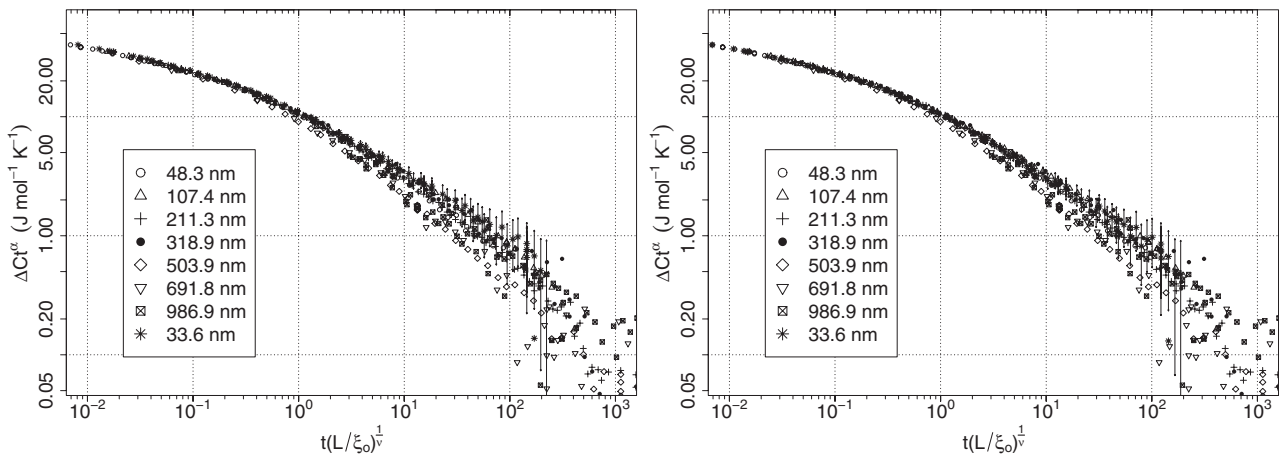

(a) Analyzed as a 33.6 nm film

(b) Analyzed as a 30 nm film

FIG. 5. Specific-heat scaling data for planar ^{4}He films above T_λ. Two analyses, (a) and (b), of the current film are shown (see text for discussion).

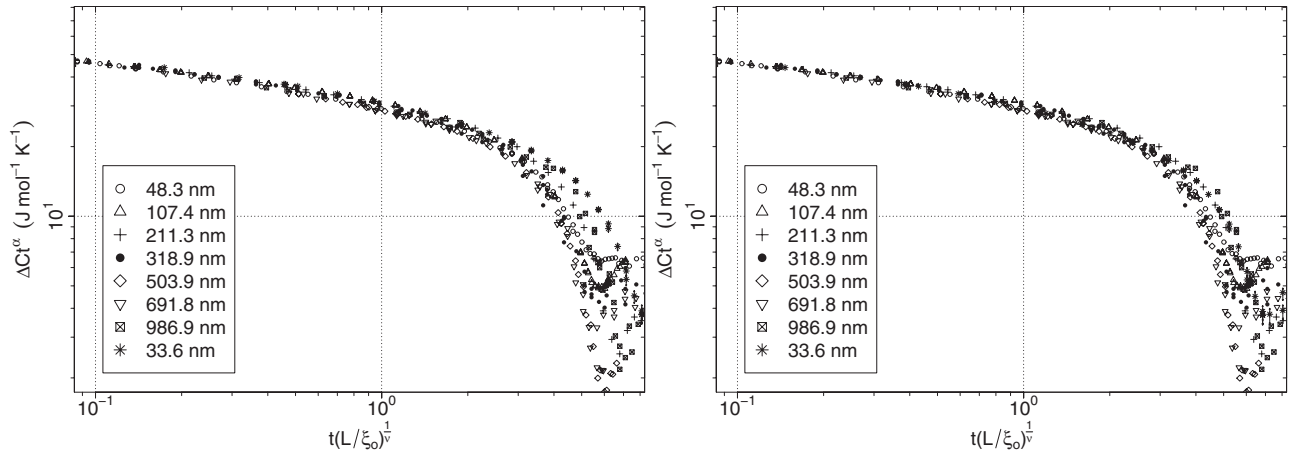

(a) Analyzed as a 33.6 nm film (b) Analyzed as a 30 nm film

FIG. 6. Specific-heat scaling data for planar ^{4}He films below T_λ. Two analyses, (a) and (b), of the current film are shown (see text for discussion).

conclusions since all our wafers are processed in the same way and any native oxide will be present on all the wafers. With this in mind, we have characterized all films using the as-grown oxide thickness as the ^{4}He film thickness rather than the reduced value suggested by scaling of a uniform film. The true thickness might be an issue if future experiments are designed to explore coupling effects as a function of film thickness rather than as a function of box separation, as we have done. We also note that this 33.6-nm film is the thinnest fully confined film for which finite-size scaling of the specific heat has been verified in ^{4}He.

B. $(2\ \mu\text{m})^3$ boxes spaced 4 μm with a 31.7-nm film

The measurement of the isolated 33.6-nm film provides the reference data to compare with films of the same thickness in contact with arrays of boxes. With this intent, a confinement cell was assembled containing an array of $(2\ \mu\text{m})^3$ boxes spaced 4 μm edge to edge connected through a measured 31.7-nm film. The heat capacity of this cell was measured and the empty cell signal subtracted. The resulting heat capacity is shown in Fig. 7. The data are plotted on a semilog plot as a function of reduced temperature t for two branches, one for above and one for below T_λ. Two distinct features on the cold branch are evident. They are the specific-heat maximum of the boxes, which occurs at $t_{m,\text{box}} \simeq 1.5 \times 10^{-5}$, and a feature associated with the heat-capacity maximum of the film at $t_{m,\text{film}} = 1.4 \times 10^{-3}$. Comparing the latter with that of the isolated film, which is also plotted in Fig. 7, we see the first sign of a proximity effect. When in contact with larger regions of ^{4}He, the temperature of the specific-heat maximum of the film is shifted to a warmer temperature.

The shift in $t_{m,\text{film}}$ is mirrored in the superfluid fraction ρ_s/ρ. The AFR technique was used to measure the ρ_s/ρ of the 31.7-nm film linking the boxes. The result is shown in Fig. 8 along with the superfluid fraction of the isolated 33.6-nm film discussed in the previous section. The solid line is the ρ_s/ρ for bulk ^{4}He. We use the following representation for this:

$$\frac{\rho_s}{\rho} = At^{0.6718}(1 + Dt^{0.5})(1 - Bt + Ct^2) \qquad (5)$$

with $A = 2.471\,35$, $B = 1.267\,03$, $C = 1.083\,64$, and $D = 0.261\,611$. The first bracket represents the correction to scaling term and the second extends the representation of ρ_s/ρ to a wider temperature range. Data from Refs. 46 and 47 are used for the critical region. This is extended using the tabulated data in Ref. 48. Focusing first on the isolated film data, one sees that due to finite-size effects they deviate from the bulk data (solid line), and finally vanish at $t = 3.0 \times 10^{-3}$ below T_λ. Due to finite-velocity effects, we are not able to follow the resonance up to the true t_c, however, our measurements are very close to this and are in agreement with the prediction of the expected universal Kosterlitz-Thouless jump.[49] This can be written as

$$\Delta\rho_s = \frac{4m}{L\lambda_T^2}, \qquad (6)$$

where $\lambda_T = h/2\pi mk_BT$ is the thermal wavelength, m is the mass of a ^{4}He atom, and L is the film thickness. The jump predicted for a 33.6-nm film is indicated by the dashed

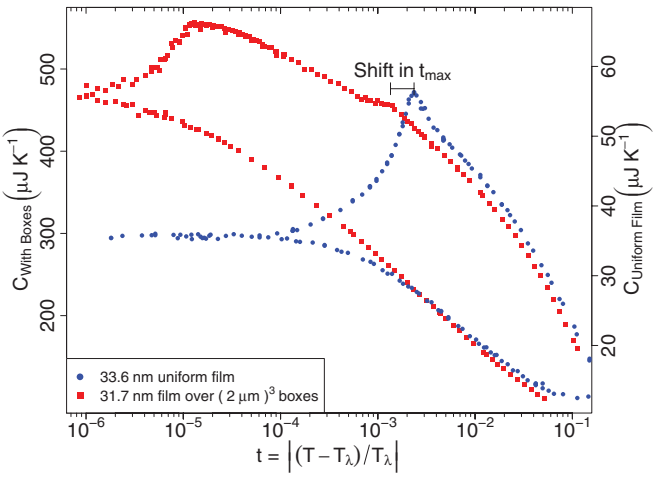

FIG. 7. (Color online) The heat capacity of ^{4}He confined in an array of $(2\ \mu\text{m})^3$ boxes spaced 4 μm edge to edge, connected through a 31.7-nm film. Also plotted on the right axis is the heat capacity of the isolated 33.6-nm film (see Fig. 4).

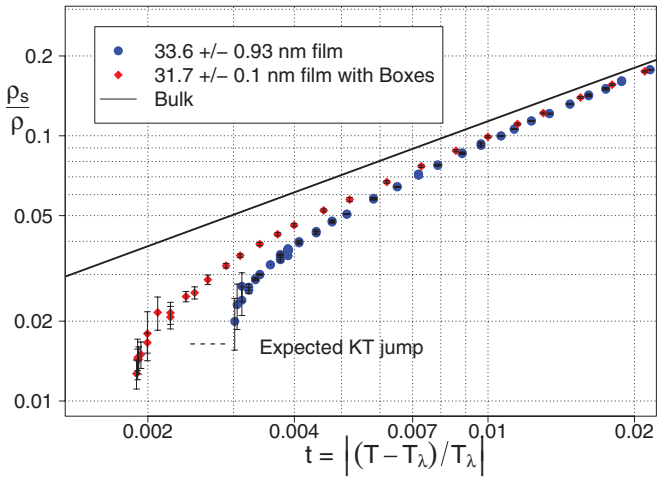

FIG. 8. (Color online) The superfluid fraction of a 31.7 ± 0.1-nm film above an array of (2 μm)^3 boxes spaced 4 μm. Also plotted are data from the 33.6-nm ^{4}He film without any boxes discussed in the previous section.

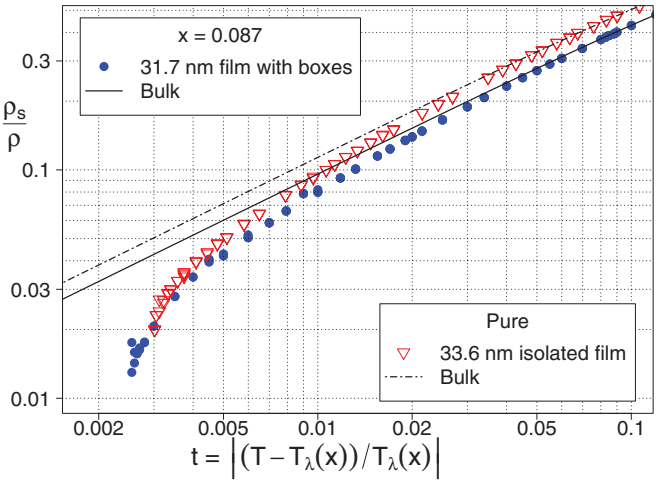

FIG. 9. (Color online) The superfluid fraction of a 31.7-nm ^{3}He-^{4}He film, $x = 0.087$, above an array of (2 μm)^3 boxes spaced 4 μm edge to edge. Also plotted are data for an isolated pure 33.6-nm film without any boxes.

horizontal line in Fig. 8. Note that if one were to take the film thickness as 30 nm, as per our earlier discussion, this dashed line would be higher by ∼10% and actually closer to the data. Focusing now on the data for the film above the array of boxes, we see that they are clearly enhanced in magnitude throughout the region surrounding $t = 3.0 \times 10^{-3}$. Not only is the magnitude enhanced, but the superfluid onset t_c is shifted in a similar way to the specific-heat maximum $t_{m,\mathrm{film}}$. The onset for the isolated film is 3.0×10^{-3} and shifts to 1.8×10^{-3} when the film is in contact with the array of boxes. The enhanced ρ_s/ρ, the shift in t_c, and the shift in $t_{m,\mathrm{film}}$ occur at temperatures where the separation of the boxes is up to 145 times $\xi^-(t)$, much farther than one would expect on the basis of any proximity theory. We note that the specific heat and superfluid density are independent measurements.

To investigate whether $\xi(t)$ is relevant to these effects, an 8.7% mixture of ^{3}He in ^{4}He was measured in this cell. Adding ^{3}He to ^{4}He increases the magnitude of the correlation length at the transition. Specifically, the correlation length is given by[50–52]

$$\xi^-(t) = \frac{2\pi m}{\lambda_T^2 \rho}\left(\frac{\rho}{\rho_s}\right) = \xi_0^- t^{-\nu}, \tag{7}$$

where ρ is the density of the liquid and ρ_s/ρ behaves to leading order as

$$\frac{\rho_s}{\rho} = k(x)t^{\nu}. \tag{8}$$

Thus, the amplitude of the correlation length prefactor at small concentrations x is given by

$$\frac{\xi_0^-(x)}{\xi_0^-(0)} = \frac{T_\lambda(x)\rho(0)k(0)}{T_\lambda(0)\rho(x)k(x)}. \tag{9}$$

If the enhanced ρ_s/ρ is related to the correlation length, then the larger correlation length in the mixture $\xi(t,x)$ should result in a larger enhancement. Plotted in Fig. 9 is the superfluid fraction of the 8.7% mixture in the film region above (2 μm)^3 boxes as well as data from the isolated 33.6-nm pure ^{4}He film. The solid and dashed-dotted lines represent ρ_s/ρ of pure bulk ^{4}He given by Eq. (5) and the ρ_s/ρ of a bulk 8.7% mixture, respectively. The bulk mixture line is given by the parametrized equations of Ref. 9. Both sets of data follow similar trends, deviating from the bulk behavior before vanishing at their respective t_c's. There are no data for an isolated 8.7% ^{3}He film 31.7 nm thick, nor an empirical scaling function that could be used to calculate this, so it is impossible to quantify the overall enhancement in the mixture data. However, t_c of the mixture is slightly smaller than that of the isolated pure film. Although the reduced temperatures in each data set are calculated relative to their own T_λ's, it is still expected that the longer $\xi(t,x)$ will result in a larger t_c for the mixture, i.e., the filled circles would be expected to have a t_c to the right of the triangles. Thus, these data also give evidence of a proximity effect. As with the pure case, this effect is also mirrored in the heat-capacity measurement shown in Fig. 10. The larger $\xi(t,x)$ would normally result in a larger depression of $t_{m,\mathrm{film}}$, however, the mixture's $t_{m,\mathrm{film}}$ is smaller than in the isolated pure ^{4}He case. This is indicated by the small kink in the open circles data of Fig. 10. Since one can not quantify the overall enhancements in the mixture data by comparing them to a uniform film of the same concentration, no quantitative analysis can be made regarding the effect of the longer $\xi(t,x)$. However, we can say that the enhancements observed in the pure film are qualitatively retained in the case of the mixture in both the superfluid density and specific heat.

Further analysis of the pure ^{4}He heat capacity shown in Fig. 7 is possible if first one accounts for the contribution of the film region. The best way to do this is to use the measured specific heat of an isolated film of near identical thickness, shown in Fig. 4, and calculate what the heat-capacity contribution of such a film in the geometry with the boxes would be. It is important to note that this assumes that the film region of this cell contributes the same amount to the signal as an isolated film of equal thickness. The remaining signal is then converted to a specific heat by dividing by the number of moles in the box region as calculated from the geometry. The data are

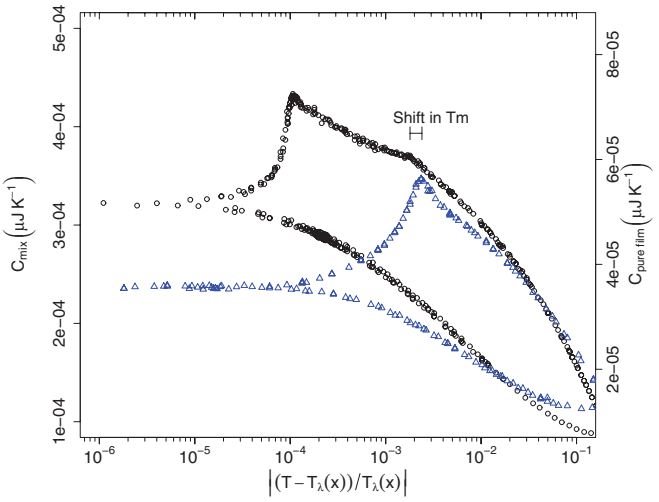

FIG. 10. (Color online) The heat capacity of an 8.7% ^{3}He-^{4}He mixture in $(2\ \mu\text{m})^3$ boxes separated 4 μm and connected through a 31.7-nm film. Plotted on the right axis is the heat capacity of a 33.6-nm isolated pure ^{4}He film.

further normalized to the bulk specific heat in the temperature region of $8 \times 10^{-4} \lesssim t \lesssim 8 \times 10^{-3}$ on the warm side of T_λ by multiplying all data by 1.009. This 0.9% correction accounts for the uncertainty in the absolute value of the specific heat as discussed previously. The result of this analysis is shown in Fig. 11. Also plotted are data from a previously measured cell where $(2\ \mu\text{m})^3$ boxes were spaced 2 μm edge to edge but connected through channels only 10 nm thick.[17] There is very good agreement between the two sets of data with perhaps some small systematic difference immediately above T_λ near $t \simeq 10^{-5}$. However, there is a clear region surrounding $t_{m,\text{film}}$ where the data sets deviate systematically. This is highlighted in the inset. Recall that during the analysis we accounted for the film region by subtracting the expected contribution

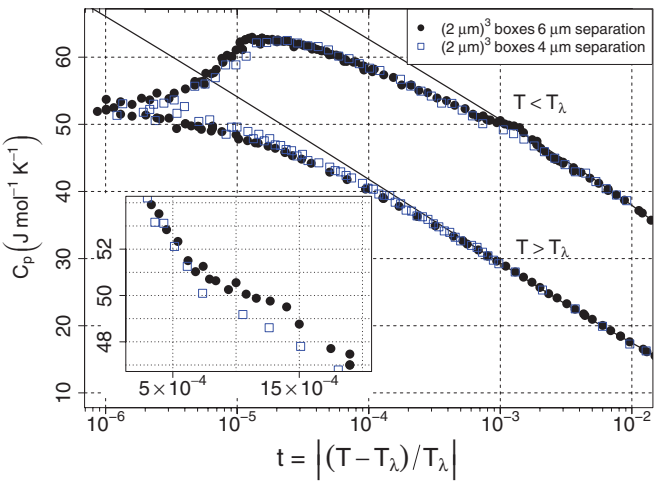

FIG. 11. (Color online) The specific heat of an array of $(2\ \mu\text{m})^3$ boxes spaced 6 μm center to center. Also plotted are data from a second array of $(2\ \mu\text{m})^3$ boxes spaced 4 μm and connected through 10-nm channels. The inset shows a region where the analysis of the current data fail to account for the signal of the connecting film (see text for details).

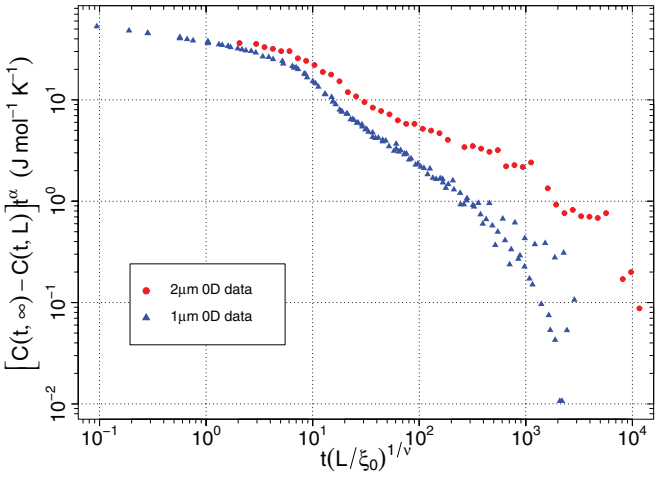

FIG. 12. (Color online) Scaling result from Ref. 2 of the specific heat for zero-dimensional confinements below T_λ. The failure of scaling is clear, with the data falling on separate loci. This lack of scaling can now be attributed to the $(1\ \mu\text{m})^3$ box data (see text for details).

determined from the specific heat of an *isolated film*. The deviation shown in the inset implies that this was not accurate, and that the specific heat of the film in contact with the much larger boxes is enhanced above that of an isolated film of equal thickness. The enhancement is another proximity effect observed on the film. As with the previous effects, this is very surprising considering at this temperature the bulk correlation length is $\xi^-(t = 1.5 \times 10^{-3}) = 27$ nm, only ~0.7% of the spacing between the boxes.

Since the two arrays of boxes have rather different connecting regions, one a 31.7-nm film, the other 2 μm × 2 μm × 10 nm channels, the overall agreement (apart from where the film orders) suggests that both measurements represent truly isolated boxes. Measurements of an array of $(1\ \mu\text{m})^3$ boxes had been tested against finite-size correlation-length scaling with the $(2\ \mu\text{m})^3$ boxes connected via channels.[2,53] The result was a lack of scaling throughout the critical region as shown in Fig. 12 for $T < T_\lambda$. The total failure of scaling on both sides of the transition is contrary to the results of all other geometries where scaling was tested.[2] Having shown now that the $(2\ \mu\text{m})^3$ boxes act as isolated entities, and considering that the $(1\ \mu\text{m})^3$ boxes were connected by channels twice as thick and half as long as the $(2\ \mu\text{m})^3$ boxes, one may conjecture that the lack of scaling is the result of an enhancement in the specific heat of the $(1\ \mu\text{m})^3$ boxes due to coupling through the connecting channels. The scaling equation for the specific heat is given by Eq. (4). One can force scaling between the $(1\ \mu\text{m})^3$ and $(2\ \mu\text{m})^3$ data by subtracting the excess specific heat due to coupling C_{coupling} which one must attribute to the $(1\ \mu\text{m})^3$ data. This excess contribution is calculated via

$$c_{\text{coupling}} = t^{-\alpha}[g_1(x)|_{2\ \mu\text{m}} - g_1(x)|_{1\ \mu\text{m}}] \qquad (10)$$

and is shown in Fig. 13. The enhancement amounts to ~6 J/mol K at the maximum and is the first evidence of a coupling effect between neighboring boxes of helium connected through weak links. We note that this is calculated not only for the superfluid side of T_λ, but also above T_λ. Furthermore, it is observed well beyond $t = 3 \times 10^{-4}$ where the separation of the boxes S is much larger than $\xi^+(t)$, i.e.,

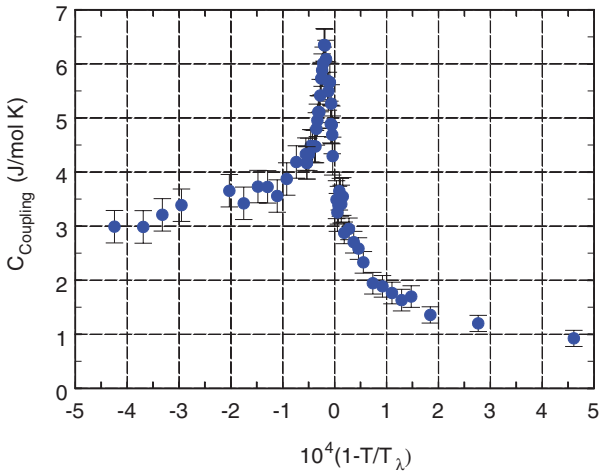

FIG. 13. (Color online) The needed excess or enhancement of the (1 μm)^3 data in order to explain the lack of scaling with data for (2 μm)^3 boxes. This enhancement is calculated using Eq. (10).

$S \simeq 30\xi(t)$. We also note that in all of this region the helium in the connecting channels is normal.

Thus, not only has the measurement of the array of (2 μm)^3 boxes connected through the 31.7-nm film revealed several effects on the film, it has also allowed us to, in conjunction with a second set of data for (2 μm)^3 boxes, deduce an enhancement in the specific heat of (1 μm)^3 boxes by imposing finite-size scaling. It has also provided a measurement of isolated (2 μm)^3 boxes that can be used as a baseline to compare with other (2 μm)^3 measurements. This will be used in the following section where the boxes in the array are brought even closer together.

C. (2 μm)^3 boxes spaced 2 μm with a 32.5-nm film

Another confinement cell in this series of measurements was fabricated with a 32.5 $\pm$ 0.98-nm film as determined from the grown oxide thickness, and an array of (2 μm)^3 boxes spaced 2 μm edge to edge. The processing of the top wafer was exactly the same as for the previous confinement. However, the pattern of the boxes had one important difference. In the fabrication of the array of boxes, the exposure field of the reduction stepper was increased. This means less exposures are required to complete the array and, more importantly, the outer edge of the array deviates from the more circular pattern of the previous cell. Thus, upon bonding, this pattern forms a uniform film outside the box array. This is shown Fig. 14. As can be seen from this figure, there are three different regions in this cell, each with their own thermodynamic signatures: the film region above the boxes, the film region outside the array of boxes, and the boxes themselves.

The heat capacity of this cell was measured and converted to a specific heat in the same manner as the previous cells where it was assumed that the film regions behaved in the same manner as an isolated film. The result is plotted in Fig. 15 along with the isolated (2 μm)^3 box data from both of the cells discussed in the previous section. The combination of these three independent measurements of (2 μm)^3 boxes show, without any assumptions involving scaling, a large enhancement in the specific heat due to coupling between the boxes when

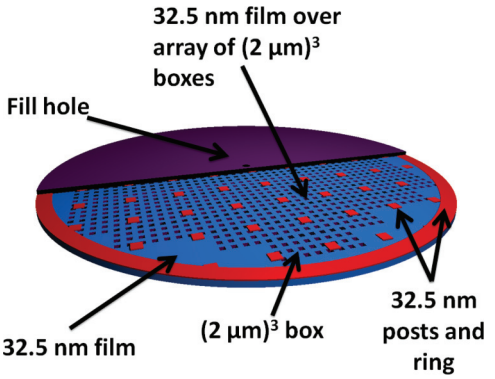

FIG. 14. (Color online) The confinement cell geometry with the (2 μm)^3 boxes spaced 2 μm edge to edge. The cell contains three different regions each with their own thermodynamic signatures (see text for details).

spaced 2 μm apart and separated via a 32.5-nm film. The enhancement, emphasized by the shading, is observable out to $t \simeq 10^{-3}$ below T_λ and $t \simeq 5 \times 10^{-4}$ above T_λ. At these temperatures, the separation of the boxes is 85 and 57 times $\xi^-(t)$ and $\xi^+(t)$, respectively. We also note that over most of this range, including part of the region below T_λ, the film connecting the boxes is not superfluid (see below). The long horizontal line in Fig. 15 at 61 J/mole K represents the expected value of C_p at T_λ for a film 2 μm thick. This would be the ultimate limit if the boxes were to be moved arbitrarily close.

The anomalously long-range enhancement in the specific heat of the boxes is paired with a similarly long-range effect in the superfluid fraction. As mentioned above, this cell defined three separate regions including a 32.5-nm film above the (2 μm)^3 box array and a 32.5-nm film isolated from any boxes. When the AFR technique was used, multiple resonances were detected. These could be attributed to one of the two film regions. Given the geometry of the cell, the resonance from the film at the perimeter can only be detected if the intervening film over the boxes is already superfluid. Plotted as filled

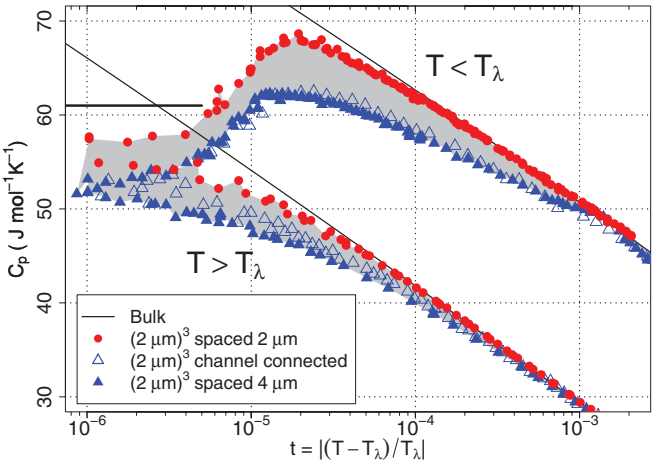

FIG. 15. (Color online) The specific heat of (2 μm)^3 boxes. When spaced 2 μm edge to edge and connected through a 32.5-nm film, the data are greatly enhanced over separate measurements of isolated (2 μm)^3 boxes. The long horizontal line is the expected value of c_p at T_λ for a planar 2 μm film.

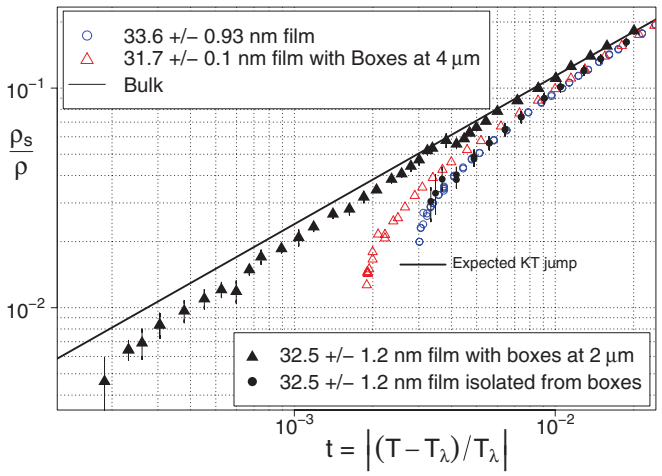

FIG. 16. (Color online) The superfluid fraction of nominally 32-nm-thick ^{4}He films. The triangles are enhanced due to a proximity effect with $(2\ \mu\text{m})^3$ boxes, while the circles are isolated from such an effect. The filled symbols were both measured in the same cell.

circles in Fig. 16 is the superfluid fraction from the perimeter region isolated from any boxes. These data fall exactly on the same locus as the isolated 33.6-nm film discussed earlier and measured in a separate experiment. This remarkable agreement attests not only to our interpretation of the multiple resonances, but also to the accuracy and consistency of our fabrication processes. It also removes any doubts that may arise from the small differences in the film thickness from cell to cell, showing that any possible effects due to this are clearly negligible relative to the proximity-coupling effects we are observing. Also plotted in Fig. 16 is the superfluid fraction calculated from the resonance associated with the film above the boxes. This resonance persists to $t \simeq 1.8 \times 10^{-4}$. Not only does ρ_s/ρ persist to a much warmer temperature (a full decade closer to T_λ) but, as was the case with the previously measured proximity-affected film, there is a large enhancement in ρ_s/ρ throughout the temperature region surrounding t_c. The enhancement is first discernible at $t \sim 2.5 \times 10^{-3}$ where $\xi(t)$ is only 19 nm.

To gauge just how unexpected these results are, we used the results of Refs. 15 and 54. These authors used a mean-field approach to the superfluid transition called Ψ theory to develop equations for the superfluid fraction at the interface between bulk ^{4}He and a film. Figure 17 shows the solution to their equations for ρ_s/ρ as a function of t, and the distance x from the interface. We used a film 32 nm thick for the numerical calculations. The results show that the effects caused at the interface are only observable within a few $\xi(t)$ from the interface.[21] A geometry closer to our box-film-box confinement is a bulk-film-bulk geometry. This geometry was also considered by the authors of Refs. 15 and 54. Applying their equations to a 32-nm-thick film region does show enhancements in the film region, however, these enhancements are only seen for very short films (64 nm long between the bulk regions). When applied to the 2000- and 4000-nm spacing between bulk regions used in our experiments, these equations result in unphysical (imaginary) solutions. Thus, this theory does not describe our experimental observations.

With theory unable to explain the distances over which these effects are observed, and the fact that theories use $\xi(t)$ as the primary length scale, an obvious question that arises is as follows: "Is $\xi(t)$ the length scale relevant in these effects?" To address this question, more analysis was performed on the data of Figs. 15 and 16.

The enhancement observed in the specific heat δc_p of the $(2\ \mu\text{m})^3$ boxes spaced at 2 μm can be quantified by subtracting from the enhanced data the data representing isolated boxes. The result, which amounts to a maximum of almost 10% of the specific heat, is plotted in Fig. 18 on a linear scale. This figure, very similar to Fig. 13 for the $(1\ \mu\text{m})^3$ boxes, shows the overall magnitude of the coupling, but does not reveal any information regarding a relevant length scale. However, when the same data are plotted on a log-log scale, as in Fig. 19, we see an interesting temperature dependence. On the warm side of T_λ, at large t's, δc_p follow a $t^{-\nu}$ temperature dependence which

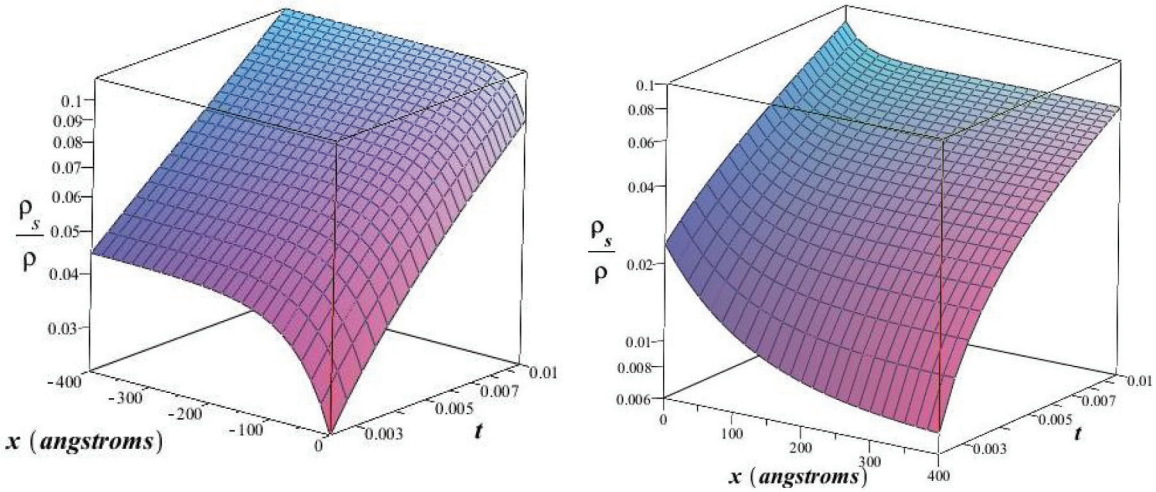

(a) Bulk Region (b) Film Region

FIG. 17. (Color online) A calculation of the superfluid fraction as a function of t and the spatial distance x near the interface between a bulk region and 32-nm film region of ^{4}He. $x < 0$ is the bulk region while $x > 0$ is the film region. The calculation applies the equations of Refs. 15 and 54, which are developed from Ψ theory.

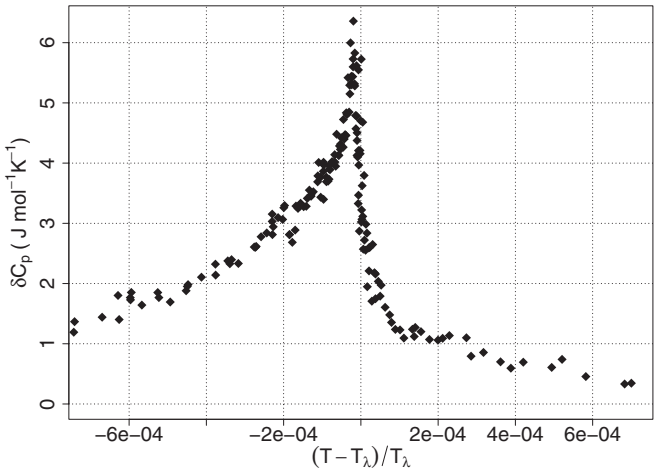

FIG. 18. The enhancement in the specific heat of the $(2\ \mu\text{m})^3$ boxes due to coupling δc_p.

is indicated by the solid line. As T_λ is approached, δc_p deviates from this dependence and rolls off to a near constant value near $t \simeq 10^{-6}$. If we consider the cell geometry, we realize that this result supports the idea that the correlation length is indeed the relevant length scale in this effect. Our cell defines a finite-size system and therefore it is not the bulk correlation length $\xi(t)$ that is relevant but the finite-size correlation length in the boxes $\xi(t,L)$, with $L = 2\ \mu$m, the size of the small dimension in the boxes. The temperature dependence of δc_p mirrors what one would expect for $\xi(t,L)$. Far from T_λ where the $\xi(t)$ is still small, finite-size effects are not observable, i.e., $\xi(t) \simeq \xi(t,L)$, and the $t^{-\nu}$ power law, indicated by the solid line, is followed. As T_λ is approached and the correlation length grows, $\xi(t)$ and $\xi(t,L)$ begin to differ. The finite size of the system prevents $\xi(t,L)$ from diverging and causes it to roll off to a finite value. This behavior is represented qualitatively by the dashed line in Fig. 19. The remarkable similarity between the temperature dependence of δc_p and the expected behavior of $\xi(t,L)$ implies that not only is $\xi(t,L)$ relevant, but $\delta c_p \propto \xi(t,L)$. However, there is an issue that needs to be addressed. The divergence of $\xi(t)$ goes as $\xi^{\pm}(t) = \xi_0^{\pm} t^{-\nu}$, where $\xi_0^+ = 0.143$ nm above T_λ and $\xi_0^- = 0.343$ nm below. This means that if our data are proportional to $\xi(t,L)$, then far from T_λ the data above and below the transition should be positioned as the ratio $\xi_0^-/\xi_0^+ = 2.40$. The upper solid line in Fig. 19 represents the expected position of δc_p far from T_λ on the cold side. Clearly, the data systematically deviate from this upper line. The deviation is, however, understandable. Recall that in the analysis of the specific heat the film region of this cell was accounted for by considering the film to have the same specific heat of an isolated film of the same thickness. We have already shown that this is not the case for the situation where the boxes were even farther apart. Thus, there is every reason to expect that in the present geometry the film would be affected even more dramatically. Thus, this deviation from the line is caused by the enhancement and shift in the specific-heat maximum of the film region between the boxes. This is clear when one compares the position of the deviation relative to the superfluid onset of the film indicated by the vertical line in the plot. It is well known that in all cases, t_c and t_m are always very close to each other, and in the thermodynamic limit identical. Our data show that the peak of the deviation from the expected line is nearly coincident with t_c of the film above the boxes. This is shown more clearly in Fig. 20 where we plot the difference between δc_p and the expected line for $T < T_\lambda$. Also plotted on the right axis as solid squares is the superfluid fraction of the film. One can see that the maximum from the film is nearly coincident with the vanishing of ρ_s/ρ. Thus, the behavior of the data below T_λ is a convolution of the two enhancements. Above T_λ there is only an enhancement in the specific heat of the boxes and the data have the same temperature dependence as $\xi(t,L)$. As one cools through the transition and approaches the temperature where the film orders, there is an additional enhancement from the film region, hence the deviation from the $\xi(t,L)$ behavior.

If the coupling is proportional to $\xi(t,L)$, then the enhanced specific heat of the $(1\ \mu\text{m})^3$ boxes inferred from scaling, as discussed earlier and shown in Fig. 13, should also follow the same trend. Figure 21 shows that when plotted in the same way, as in Fig. 19, this is the case. One can not analyze the data for

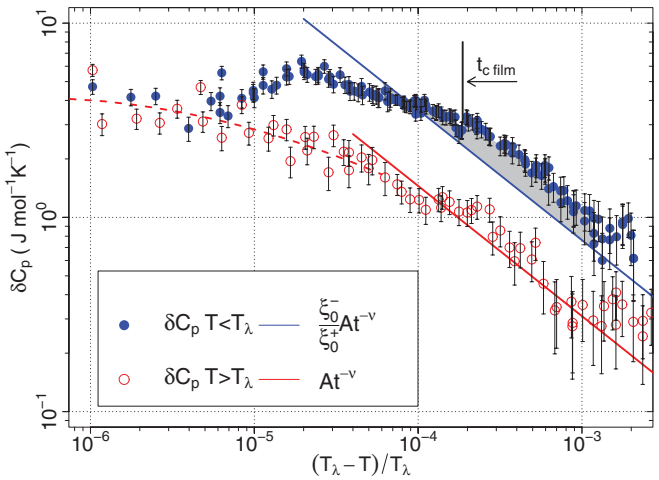

FIG. 19. (Color online) The enhancement in the specific heat of the $(2\ \mu\text{m})^3$ boxes due to coupling δc_p plotted on a log-log scale. The superfluid onset temperature t_c of the 32.5-nm film above the boxes is indicated with a vertical line.

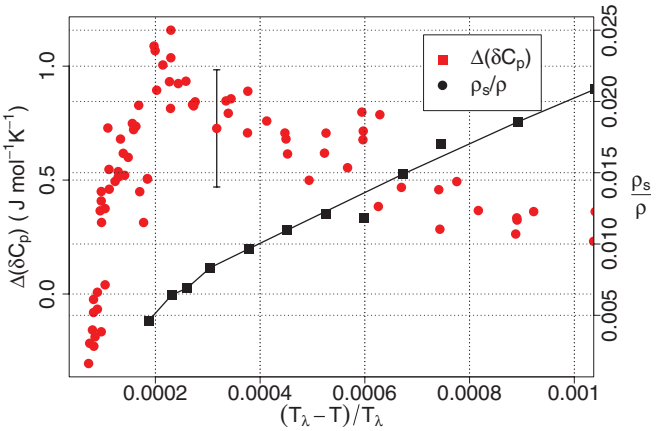

FIG. 20. (Color online) The deviation $\Delta(\delta c_p)$ of δc_p from the line shown in Fig. 19. This line indicates the expected behavior based on a proportionality to $\xi^-(t,L)$. The superfluid fraction of the film above the $(2\ \mu\text{m})^3$ boxes is plotted on the right axis. The peak in $\Delta(\delta c_p)$ is nearly coincident with the vanishing of the superfluid fraction.

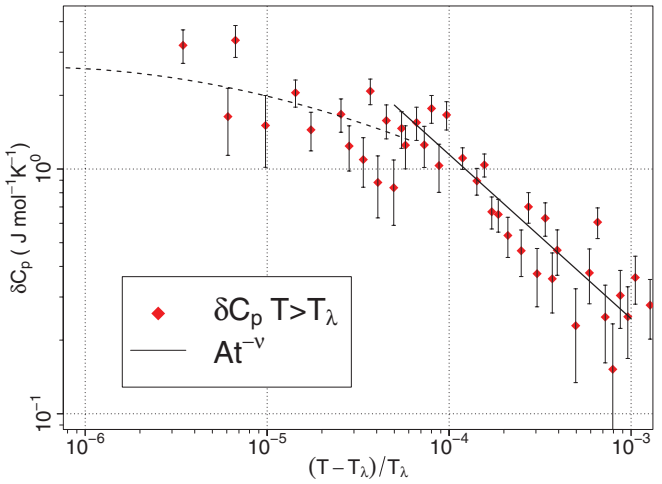

FIG. 21. (Color online) The enhancement in the specific heat of the $(1\ \mu\text{m})^3$ boxes due to coupling δc_p as inferred from scaling.

$T < T_\lambda$ in the same way since scaling fails near the specific-heat maximum.[2] To obtain a plot similar to Fig. 19 for $T < T_\lambda$, one would need to do a separate experiment where the $(1\ \mu\text{m})^3$ boxes are moved farther apart so that they act as isolated units.

A similar analysis as for δc_p can be performed on the enhanced superfluid fractions shown in Fig. 16. Where there are data for the isolated film, i.e., for temperatures below its superfluid onset, they can be subtracted from the enhanced ρ_s/ρ of the films which are subject to proximity effects. The result is plotted in a log-log plot shown in Fig. 22. The enhancement of the film above the boxes spaced 4 μm, the open triangles, is in very good agreement with the $t^{-\nu}$ power law indicated by the line. The data for the film above the boxes spaced 2 μm, the filled triangles, is noisier and have some clear deviations but are still consistent with the power law. It should be noted that there is no rounding off of the power law as in the heat capacity; this is because in this temperature region, below the superfluid onset of the film, the boxes are still bulklike and have not yet experienced any significant finite-size effect rounding of the correlation length. This analysis for the superfluid density, as well as that of Fig. 19

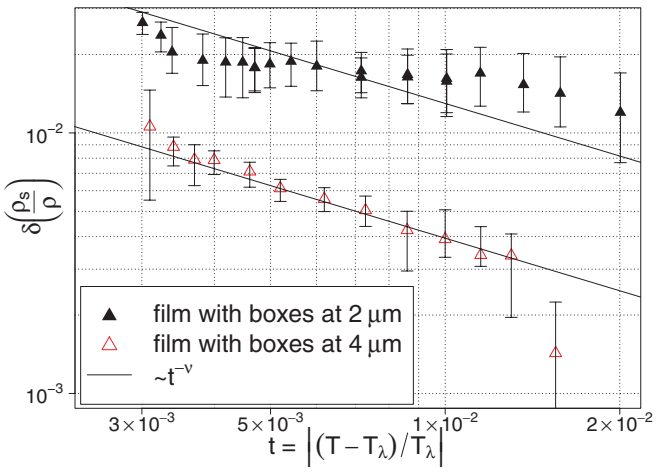

FIG. 22. (Color online) The enhancement in the superfluid fraction of the coupled films. The solid lines indicate a $t^{-\nu}$ dependence.

for the specific heat, are strong support for $\xi(t,L)$ being the relevant length scale in these effects.

D. $\xi(t,L)$ and its scaling

Having shown evidence that the enhancements are proportional to $\xi(t,L)$, we can now use δc_p to learn more about $\xi(t,L)$. Like other thermodynamic responses, the correlation length of a finite-size system should be described by a scaling function f such that[55]

$$\frac{\xi(t,L)}{\xi(t,\infty)} = f\left(\frac{L}{\xi(t,\infty)}\right). \tag{11}$$

This can also be written in a, perhaps, more intuitive way using another scaling function X, i.e.,[56]

$$\xi(t,L) = LX\left(\frac{L}{\xi(t,\infty)}\right). \tag{12}$$

The δc_p data can be used to actually map out X within a multiplicative constant and test these scaling predictions. For scaling to hold, both the δc_p data for $(1\ \mu\text{m})^3$ and $(2\ \mu\text{m})^3$ boxes should yield the same value for $X(0)_{L=1\ \mu\text{m}}$ and $X(0)_{L=2\ \mu\text{m}}$ at T_λ. With $\delta c_p \propto \xi(t,L)$, we can write

$$\xi(t_a,L) = \frac{\xi(t_{\text{large}},\infty)\delta c_p(t_a)}{\delta c_p(t_{\text{large}})}, \tag{13}$$

where δc_p at t_{large} refers to the region where $\xi(t,L) \simeq \xi(t,\infty)$. In particular for $L = 2\ \mu$m and $t = 10^{-6} \simeq 0$, the δc_p data yield $\xi(0, L = 2\ \mu\text{m}) = (0.14 \pm 0.02)L$. When Eq. (13) is applied to the δc_p data for the enhancement of the $(1\ \mu\text{m})^3$ boxes inferred from the scaling of the specific heat (Fig. 21), it results in $\xi(t, L = 1\ \mu\text{m}) = (0.13 \pm 0.04)L$ at $t = 10^{-6} \simeq 0$. The agreement between these two separate measurements confirms that the data above T_λ in Fig. 19 defines the scaling function X to within a multiplicative constant which must depend on the geometry of the connecting region. Furthermore, Eq. (13) predicts that the maximum length $\xi(t,L)$ achieves in the box geometry is $0.20L$. This occurs at the specific-heat maximum. Using $\xi(t,L)$ as the gauge makes the distance over which we are observing enhancements even more surprising. We also note that although there are no theoretical calculations of $X(0)$ appropriate for ^{4}He, in the case of finite Ising strips one has $X(0) = 1/2\pi \simeq 0.16$ for the energy-energy correlation length.[57]

IV. CONNECTION WITH OTHER HELIUM MEASUREMENTS

When considering helium near the superfluid transition in a heterogeneous confinement, one of the first considerations might be the distribution of confinement regions. Our work indicates that it is just as important to consider the coupling among these regions. This mutual influence of two coexisting regions of helium has a direct bearing on many observations in experiments where helium is confined in porous media. While the geometry in many of these cases is not well defined, there are features in the data that are indicative of the behavior we have identified with our boxes-film geometry.

Experiments on helium confined in porous glasses and packed powders represent a heterogeneous confinement that is

outside the description of finite-size scaling. This requires that the confinement be uniform and characterized at its simplest by a single length scale. In such heterogeneous media, there is a distribution of length scales that differ for each system. Some of the data for ^{4}He confined in such systems have been reviewed in Refs. 2 and 5. In particular, measurements of the superfluid density in porous glasses, Vycor, xerogel, and aerogel, have shown that one can represent data as a power law relative to the local transition temperature for each confinement.[58] However, these power laws differ for each porous medium (see Table I of Ref. 5). Also, in the case of aerogel, data have been obtained as function of pressure which show that the exponent is universal provided one allows for correction to scaling terms in the power-law description.[59] In the case of aerogel, measurements with different glass density show that the exponent for the superfluid fraction is dependent on this density. Our work brings a new aspect to the understanding of these systems. Specifically, one expects that not only the distribution in the sizes of the heterogeneous confinement would be important, but also their connectivity. Our measurements show that proximity effects are manifest over very large distances, thus, large confinement regions can affect smaller regions to a much greater extent than one might have anticipated on the basis of just the magnitude of the correlation length. We also point out that a pure power-law dependence in the superfluid density does not necessarily indicate a new universality class, but might just be a reflection of a particular type of confinement. We can illustrate this with our own data for the superfluid density of films in equilibrium with boxes (see Fig. 16). This system is heterogeneous but consisting of only two well-defined geometric confinements. If one were to plot the superfluid density of the film on a scale of $T - T_c$ instead of $T - T_\lambda$, as we have done, one would obtain a pure power law with exponent $\nu \simeq 0.69$. This could not be construed as indicating that the film acts like bulk helium with ν close to 0.67, or that it represents a new universality class, if one takes seriously the difference between 0.69 and 0.67 to be significant. On the contrary, the behavior of ρ_s/ρ can be understood, as we have demonstrated, in term of the proximity effects to the larger confinement of the boxes. We also note that measurements of ρ_s for helium confined in Nuclepore filters, discussed further below, can also be described with an exponent $\nu \simeq 0.67$ if one plots these data relative to the onset temperature for each confinement size[9,60] (see also Ref. 2 for discussion of this point relative to finite-size scaling). One would not conclude on the basis of this exponent that the confinement is bulklike.

Recently, the superfluid transition of ^{4}He in porous gold and CaF_2 has been studied in the region where a film is formed on the substrate and the partial pressure is such that a capillary condensed phase is also in equilibrium with the film.[61] The capillary phase has a much larger dimension than the film, thus this mimics to some extent our boxes-film experiment. Figure 31 in Ref. 61 is a cartoon of this geometry. The measurements involve mass loading and dissipation of a quartz crystal oscillator. This is done at fixed temperatures as a function of partial pressure or film thickness. What is observed is that if only a film exists on the substrate, one can measure both the dissipation and discontinuous mass loading associated with the Kosterlitz-Thouless (KT) transition in the film. However, in the presence of a capillary phase, the abrupt change in mass loading, which one might expect from the film, is no longer visible. It is as if the superfluid onset is more continuous rather than abrupt. This is similar to our observations that the superfluid density persists closer to the transition and has values lower than the expected KT jump, i.e., the transition is more continuous. The measurements with the quartz crystal oscillator are all for relatively thin films and can not be followed to thick films such that the power-law critical behavior near T_λ could be observed.

A number of experiments have been done with helium confined in Nuclepore filters. These are polycarbonate membranes in which ion tracks are etched to yield nearly cylindrical flow channels of different diameters. The membranes themselves are either 5 or 10 μm thick. A number of characteristics of these filters have been determined by different investigators.[62–65] Some of the experimental results for helium confined in these filters are relevant to our observations.

As shown in Fig. 7, when two characteristic sizes are present, the specific heat has two features associated with the transition in each geometry. Under suitable conditions, these transitions can influence each other as discussed above. In the measurement of the heat capacity of ^{4}He in 0.2-μm Nuclepore filters, a two-peak structure was also observed in situations where a capillary condensed phase was in equilibrium with a film of $\sim$5.5 nm.[66] One relatively sharp peak was associated with the capillary condensed phase, the other broader peak with the film in equilibrium with it. As the capillary phase was increased by condensing more helium, the maximum of the film in equilibrium with this phase moved in temperature closer to T_λ. Although it was not realized at the time, this movement towards T_λ is much too large to be explained by a convolution or blending of the two signals coming from the films and the capillary phase (see Fig. 7 of Ref. 66). It is very likely that the capillary condensed phase (the large region analogous to helium in the boxes) influenced the transition in the film and caused it to move to higher temperatures. The cylindrical pores of Nuclepore filters do not have smooth surfaces. Further, there are internal links among the pores that further complicate the geometry.[63] Also, there are no data for a perfectly planar 5.5-nm film that one could subtract in order to analyze the residual signal due to coupling. However, is seems very likely that these early observations are also an indication of proximity effects between the capillary condensed region and the film. On this issue of two-peaks signal in the heat capacity, we also note that calculations on a "layered" 2D Ising model yield a two-peaks structure reflecting order within a layer and a more global order across the 2D system.[67]

The magnitude of the specific heat for helium filling Nuclepore filters might also be indicative of enhanced behavior due to coupling from pore to pore. When these data are compared with other, better controlled cylindrical confinement (1D crossover), one finds that the Nuclepore specific heat close to the transition is consistently higher in magnitude than for other realizations of 1D confinement. This was discussed in Ref. 2 (see in particular the scaling plots of Figs. 35 and 36). Thus, they define a slightly different scaling locus from the rest of the 1D data. The pore separation in these filters is between 40 and 50 μm; this is too far for coupling through a saturated film. However, as mentioned above, a fraction of these pores cross[65]

which would certainly lead to coupling among the pores and an enhancement of the specific heat. In resonance experiments to determine the superfluid fraction, these filters would be surrounded by bulk liquid.[60] However, with filters thickness of 5–10 μm, it would not seem likely that there would be a large enhancement due to the presence of bulk liquid at both ends of the pores. However, the crossing of channels might provide such a mechanism as the scaling plots of the specific heat suggest. There are no benchmark data for the superfluid density in isolated and longer channels with which these data could be compared to deduce the magnitude of enhancement.

Josephson effects have been measured in ^{4}He using arrays of slits 0.17 μm high[6] or circular pore apertures of diameter ~ 50 nm.[7] The arrays in these experiments allow one to obtain a measurable mass flow upon imposing a chemical potential different across them. These experiments make use of the growth of the correlation length near T_λ to make measurements in a regime where the slits or apertures act as weak links. In the case of Ref. 6, it is pointed out that the ideal Josephson regime is achieved only for temperatures closer than $T_\lambda - T \leqslant 100$ μK. For their slit geometry, one would expect the critical temperature for superfluid onset in the slit to be $T_\lambda - T_c \simeq 430$ μK. Thus, they are observing effects in a region where the helium in the slits should be normal. Similarly, in Ref. 7, Josephson oscillations are seen at $T_\lambda - T = 0.8$ mK whereby the critical temperature for the circular apertures should be at $T_\lambda - T \simeq 2.3$ mK. Therefore, in both experiments one obtains superflow in a temperature region where the helium in the isolated weak links should be normal. Both of these experiments are thus relying on proximity effects, due to the surrounding bulk liquid, to maintain a nonzero order parameter in the weak links.

Studies of the specific heat of ^{3}He-^{4}He mixtures show very anomalous behavior for 0D crossover in $(1\ \mu\text{m})^3$ boxes that is very likely due to coupling effects.[68] When ^{3}He is introduced in ^{4}He, the superfluid transition shifts to lower temperatures and, at fixed concentration x, the specific heat $C_{px}(t)$ is renormalized to a progressively weaker cusp.[69] True criticality is only observed in $C_{p\phi}$ where ϕ is the difference in the chemical potentials $\phi = \mu_3 - \mu_4$.[36] The amplitude of the correlation length in the mixtures $\xi_0(x)$ increases with concentration, doubling from $x = 0$ to $x \simeq 0.4$ [see Eq. (9)]. In a finite system of small dimension L, this doubling of $\xi_0(x)$ implies that, for the same confinement L, finite-size effects will onset sooner in the mixtures than in pure ^{4}He. This was tested for 2D and 1D crossover with reasonable scaling results.[17,70] However, for $(1\ \mu\text{m})^3$ boxes and 0D crossover, completely different results were obtained. Specifically, with both C_{px} and the calculated $C_{p\phi}$, the specific heat exceeded the bulk values near the maximum by a substantial amount. Also, the maximum shifted to lower temperatures much more rapidly with concentration than for the 2D and 1D confinement. Given that for pure ^{4}He the $(1\ \mu\text{m})^3$ cell has been demonstrated now to show box-to-box coupling, it seems reasonable to ascribe this behavior to an enhanced coupling due to an increase in $\xi_0(x)$. However, this does not explain in detail the temperature dependence of either C_{px} or $C_{p\phi}$. To do this, one would need a series of experiments where the $(1\ \mu\text{m})^3$ boxes are placed farther apart, and are uncoupled. This would establish the baseline of the uncoupled response.

V. CONNECTION WITH OTHER SYSTEMS

The correlation length is not a parameter unique to ^{4}He. The evidence that the effects we have reported here are dependent on $\xi(t,L)$ suggests that there should be some universal physics involved and that other critical systems may show analogous effects. One of the most obvious candidates for this is the high-temperature superconductor (HTSC) cuprate system. The HTSC cuprates have a very small zero-temperature correlation length, much like ^{4}He, which implies a critical region dominated by fluctuations. Recent measurements of junctions composed of an underdoped cuprate layer sandwiched between optimally doped leads have shown coupling effects on a very large length scale.[71,72] The doping of the layers was such that the transition temperature of the central layer T_c is lower than that of the leads T_c'. In Ref. 71, measurements are reported of the familiar Josephson effects in these junctions with a central layer much thicker than could be expected based on conventional theories. In Ref. 72, muon spin resonance is used to probe the local magnetic field and showed that the Meissner effect occurred in the central layer at a temperature higher than T_c. These effects, coined "giant proximity effects," have led another group to pursue analogous effects in semiconducting ferromagnets (EuS, EuO) and ferromagnetic metals.[73] Another system to consider is the Bose-Einstein condensate (BEC) system. Much like ^{4}He, this system has a wave-function order parameter, and the bulk correlation length, its critical exponent,[74] and the Josephson effects[75,76] have all been measured. Recently, measurements have been made on an ultracold gas "atomic circuit" which contains an adjustable barrier.[77] With a critical region that is experimentally accessible and the Josephson effects to gauge the strength of coupling, this atomic circuit may be an ideal system to measure these anomalous effects in BECs.

VI. SUMMARY AND CONCLUSIONS

We have reported measurements of both specific heat and superfluid density for helium in well-defined geometries. These data show coupling and proximity effects between confinement regions at distances much larger than the three-dimensional correlation length $\xi(t)$, or $\xi(t,L)$ as modified by finite-size effects. We have demonstrated, via the temperature dependence of these effects, that $\xi(t,L)$ is indeed the relevant parameter governing the coupling. However, because effects are seen at distances over 100 times $\xi(t,L)$, the observed behavior can not be explained from a mean-field approach, or from what is understood as the meaning of the correlation length: the distance over which order propagates in the critical region. We have pointed out other observations in ^{4}He experiments that are qualitatively consistent with our observations. We have also pointed out that other critical systems, where fluctuations dominate the critical response, should have similar behavior.

ACKNOWLEDGMENTS

This work was supported by the NSF Grants No. DMR-605716 and No. DMR-1101189; the Cornell Nanoscale and Technology Facility, Project No. 526-94; the Mark Diamond Research Fund of the University at Buffalo; and other internal

university funding. We also thank the University at Buffalo College of Arts and Sciences Instrument Shop and the Cryogenic Facility. One of us (F.M.G.) acknowledges the Moti Lal Rustgi Professorship endowment.

[1]G. Ahlers, in *The Physics of Liquid and Solid Helium, Part I*, edited by K. H. Bennemann and J. B. Ketterson (Wiley, New York, 1976), p. 85.
[2]F. M. Gasparini, M. O. Kimball, K. P. Mooney, and M. Diaz-Avila, Rev. Mod. Phys. **80**, 1009 (2008).
[3]M. Campostrini, M. Hasenbusch, A. Pelissetto, and E. Vicari, Phys. Rev. B **74**, 144506 (2006).
[4]F. M. Gasparini and I. Rhee, in *Progress in Low Temperature Physics*, edited by D. F. Brewer, Vol. 13 (North Holland, New York, 1992), pp. 1–90.
[5]J. D. Reppy, J. Low Temp. Phys. **87**, 205 (1992).
[6]K. Sukhatme, Y. Mukharsky, T. Chui, and D. Pearson, Nature (London) **411**, 280 (2001).
[7]E. Hoskinson, Y. Sato, and R. E. Packard, Phys. Rev. B **74**, 100509 (2006).
[8]Previously (Ref. 22), we have used $\xi_0^- = 0.352$ nm. This magnitude depends on the leading amplitude on the behavior of the superfluid density [see Eq. (7) and Refs. 9–11]. For the present value of ξ_0^- we have used the results of ρ_s from Refs. 9–11.
[9]P. C. Schubert and W. Zimmermann, J. Low Temp. Phys. **44**, 177 (1981).
[10]A. Singsaas and G. Ahlers, Phys. Rev. B **30**, 5103 (1984).
[11]L. S. Goldner and G. Ahlers, Phys. Rev. B **45**, 13129 (1992).
[12]W. Y. Tam and G. Ahlers, Phys. Rev. B **32**, 5932 (1985).
[13]K. K. Likharev, Rev. Mod. Phys. **51**, 101 (1979).
[14]J. C. Davis and R. E. Packard, Rev. Mod. Phys. **74**, 741 (2002).
[15]Y. G. Mamaladze and O. D. Cheishvili, Z. Eksp. Teor. Fiz. **50**, 169 (1960) [Sov. Phys.–JETP **23**, 112 (1966)].
[16]M. O. Kimball, Ph.D. thesis, University at Buffalo, The State University of New York, 2005.
[17]K. P. Mooney, Ph.D. thesis, University at Buffalo, The State University of New York, 2006.
[18]L. P. Kadanoff, in *Statistical Physics: Statics, Dynamics and Renormalization* (World Scientific, New Jersey, 2000), p. 232.
[19]M. E. Fisher, in *Critical Phenomena, Proceedings of the 51st "Enrico Fermi" Summer School, Varenna, Italy*, edited by M. S. Green (Academic, New York, 1971).
[20]J. K. Perron, M. O. Kimball, K. P. Mooney, and F. M. Gasparini, Nat. Phys. **6**, 499 (2010).
[21]J. K. Perron and F. M. Gasparini, J. Low Temp. Phys. **162**, 136 (2011).
[22]J. K. Perron and F. M. Gasparini, Phys. Rev. Lett. **109**, 035302 (2012).
[23]J. K. Perron and F. M. Gasparini, J. Low Temp. Phys. (to be published).
[24]Cornell NanoScale Science and Technology Facility is located at 250 Duffield Hall, Cornell University, Ithaca, New York 1853-2700.
[25]*Quick Reference Manual for Silicon Integrated Circuit Technology*, edited by W. Beadle, J. C. C. Tsai, and R. D. Plummer (Wiley, New York, 1984); see for chemical recipes used for processing Si.
[26]S. Mehta, M. O. Kimball, and F. M. Gasparini, J. Low Temp. Phys. **114**, 467 (1999).
[27]The 2000-nm target thickness is never hit exactly, but the different thickness and the effect it has on the volume of the boxes is taken into account during the analysis.
[28]I. Rhee, D. J. Bishop, A. Petrou, and F. M. Gasparini, Rev. Sci. Instrum. **61**, 1528 (1990).
[29]Constantan is an alloy consisting of a 55:45 ratio of copper and nickel, chosen for its near constant resistance at low temperatures and reliable film formation on silicon.
[30]G. McConville, Cryogenics **9**, 122 (1969).
[31]B. W. Mangum and G. T. Furukawa, National Institute of Standards and Technology Report No. 1265 (unpublished).
[32]S. M. Bhagat and R. A. Lasken, Phys. Rev. A **3**, 340 (1971).
[33]R. V. Duncan, G. Ahlers, and V. Steinberg, Phys. Rev. Lett. **60**, 1522 (1988).
[34]A. W. Harter, R. A. M. Lee, A. Chatto, X. Wu, T. C. P. Chui, and D. L. Goodstein, Phys. Rev. Lett. **84**, 2195 (2000)..
[35]F. M. Gasparini, M. O. Kimball, and S. Mehta, J. Low Temp. Phys. **125**, 215 (2001).
[36]F. M. Gasparini and M. R. Moldover, Phys. Rev. B **12**, 93 (1975).
[37]G. Ahlers, Phys. Rev. A **3**, 696 (1971).
[38]J. A. Lipa and T. C. P. Chui, Phys. Rev. Lett. **51**, 2291 (1983).
[39]T.-P. Chen and F. M. Gasparini, Phys. Rev. Lett. **40**, 331 (1978).
[40]R. W. Hill and O. V. Lounasmaa, Philos. Mag. **2**, 145 (1957).
[41]H. Kahn, C. Deeb, I. Chasiotis, and A. Heuer, J. Microelectromech. Syst. **14**, 914 (2005).
[42]M. Morita, T. Ohmi, E. Hasegawa, M. Kawakami, and M. Ohwada, J. Appl. Phys. **68**, 1272 (1990).
[43]We use $\alpha = -0.0115$ which corresponds to $\alpha = 2 - 3\nu$ and $\nu = 0.6705$ given in Ref. 11.
[44]M. E. Fisher and M. N. Barber (unpublished).
[45]J. K. Perron, Ph.D. thesis, University at Buffalo, The State University of New York, 2012.
[46]D. S. Greywall and G. Ahlers, Phys. Rev. Lett. **28**, 1251 (1972).
[47]D. S. Greywall and G. Ahlers, Phys. Rev. A **7**, 2145 (1973).
[48]J. Maynard, Phys. Rev. B **14**, 3868 (1976).
[49]D. R. Nelson and J. M. Kosterlitz, Phys. Rev. Lett. **39**, 1201 (1977).
[50]R. A. Ferrell, N. Menyhard, H. Schmidt, F. Schwabl, and P. Szépfalusy, Ann. Phys. (NY) **47**, 565 (1968).
[51]B. I. Halperin and P. C. Hohenberg, Phys. Rev. **177**, 952 (1969).
[52]M. E. Fisher, M. N. Barber, and D. Jasnow, Phys. Rev. A **8**, 1111 (1973).
[53]J. K. Perron, M. O. Kimball, K. P. Mooney, and F. M. Gasparini, J. Phys.: Conf. Ser. **150**, 032082 (2009).
[54]L. V. Kiknadze, Y. G. Mamaladze, and O. D. Cheishvili, Izmer. Tekh. **7**, 29 (1984) [Meas. Tech, **27**, 607 (1985)].
[55]E. Brezin, J. Phys. **43**, 15 (1982).
[56]V. Privman and M. E. Fisher, Phys. Rev. B **30**, 322 (1984).
[57]V. Privman, P. C. Hohenberg, and A. Aharony, in *Phase Transitions and Critical Phenomena*, edited by C. Domb and J. L. Lebowitz, Vol. 14 (Academic, New York, 1991).
[58]M. H. W. Chan, K. I. Blum, S. Q. Murphy, G. K. S. Wong, and J. D. Reppy, Phys. Rev. Lett. **61**, 1950 (1988).

[59]N. Mulders, R. Mehrotra, L. S. Goldner, and G. Ahlers, Phys. Rev. Lett. **67**, 695 (1991).
[60]J. S. Brooks, B. B. Sabo, P. C. Schubert, and W. Zimmermann, Phys. Rev. B **19**, 4524 (1979).
[61]R. J. Lazarowich and P. Taborek, Phys. Rev. B **74**, 024512 (2006).
[62]T.-P. Chen, M. J. DiPirro, B. Bhattacharyya, and F. M. Gasparini, Rev. Sci. Instrum. **51**, 846 (1980).
[63]F. M. Gasparini and S. Mhlanga, Phys. Rev. B **33**, 5066 (1986).
[64]N. Giordano, Phys. Rev. B **27**, 5447 (1983).
[65]D. T. Smith, K. M. Godshalk, and R. B. Hallock, Phys. Rev. B **36**, 202 (1987).
[66]T. P. Chen, M. J. DiPirro, A. A. Gaeta, and F. M. Gasparini, J. Low Temp. Phys. **26**, 927 (1977).
[67]M. Fisher, J. Phys. Soc. Jpn. **26**, 87 (1969).
[68]M. O. Kimball and F. M. Gasparini, Phys. B (Amsterdam) **329**, 162 (2003).
[69]F. Gasparini and M. R. Moldover, Phys. Rev. Lett. **23**, 749 (1969).
[70]M. O. Kimball and F. M. Gasparini, Phys. Rev. Lett. **95**, 165701 (2005).
[71]I. Bozovic, G. Logvenov, M. A. J. Verhoeven, P. Caputo, E. Goldobin, and M. R. Beasley, Phys. Rev. Lett. **93**, 157002 (2004).
[72]E. Morenzoni, B. M. Wojek, A. Suter, T. Proksca, G. Logvenov, and I. Bozovic, Nat. Commun. **2**, 1273 (2011).
[73]J. Goff (unpublished).
[74]T. Donner, S. Ritter, T. Bourdel, A. Öttl, M. Köhl, and T. Esslinger, Science **315**, 1556 (2007).
[75]I. Zapata, F. Sols, and A. J. Leggett, Phys. Rev. A **57**, R28 (1998).
[76]F. S. Cataliotti, S. Burger, C. Fort, P. Maddaloni, F. Minardi, A. Trombettoni, A. Smerzi, and M. Inguscio, Science **293**, 843 (2001).
[77]A. Ramanathan, K. C. Wright, S. R. Muniz, M. Zelan, W. T. Hill, C. J. Lobb, K. Helmerson, W. D. Phillips, and G. K. Campbell, Phys. Rev. Lett. **106**, 130401 (2011).